NUMERICAL STUDY OF COMPRESSIVE BEHAVIOR OF CONCRETE AT HIGH STRAIN RATES

By F. V. Donzé,[1] S.-A. Magnier,[2] L. Daudeville,[3] C. Mariotti,[4] and L. Davenne[5]

ABSTRACT: High strain rate unconfined compressional tests on concrete are simulated by a 3D discrete-element method. The laboratory data set was provided by three unconfined experiments on a split Hopkinson pressure bar apparatus at very high strain rates (350–700 s^{-1}). This numerical method was chosen because it is well adapted to problems involving the characterization of fracturing and fragmentation in geomaterials. The simulations input data are the recorded experimental velocities, whereas the simulations output data are the computed forces that are compared with the experimental ones. The fit between the experimental and the numerical data is quite good. Based on this fit, it is shown that the strain rate dependency of the material strength can be explained by inertial effects.

INTRODUCTION

Understanding the response of concrete specimens when subjected to high strain rates is essential to grasp the behavior of concrete structures involved in extreme situations such as impact loadings. It has been observed that geomaterials exhibit significant changes in their response during dynamic versus static loading phases, which is why it is difficult to use their static properties to explain their dynamic behavior. These noted changes seem to greatly affect the macroscopic properties, such as strength, stiffness, and ductility (Bischoff and Perry 1995). Their studies have shown that the uniaxial compressive strength of plain concrete increased with an increase in strain rate and that the compressive impact strength was much greater than the static strength. In other experimental data, the resistance was seen to increase rapidly at high loading rates, whereas prepeak crack growth that occurs at all loading rates decreased with increasing rates (Gopalaratnam et al. 1996).

Although the behavior of concretes at low strain rates, which range around 10^{-5} s^{-1}, seems well understood, knowledge of their high strain rate (>10^{0} s^{-1}) behavior is rather limited. The low strain rate region (i.e., static loading) is associated with creep (Bischoff and Perry 1991).

For high strain rates an important consensus seems to exist on the preponderance of two effects: (1) The viscoelastic character of the hardened cement paste; and (2) the time-dependent nature of the crack growth that is thermally activated (Gopalaratnam et al. 1996). Some authors interpret the viscous behavior that contributes to the rate dependence as being due to the presence of the free water in the material, leading to an effect similar to the Stefan effect (Rossi et al. 1994). These authors note that at strain rates ranging around 10^{0} s^{-1} samples do not seem to exhibit any loading rate dependence unless free water is present. However, their conclusions cannot explain the observed rate dependence at higher strain rates (>10^{2} s^{-1}) on dry samples.

Although the majority of authors do not consider inertia to play a major role in the rate dependence, few others argue in favor of its importance. During rapid loading, microcracks have less time available for their development or propagation. Local equilibrium is not attained, and the inertial forces, which are in opposition to the displacement, will increase the apparent resistance. Thus, an increased loading will be required before cracking becomes prominent enough to ruin the material (Bischoff and Perry 1995). Alternatively, it has been suggested that a concrete specimen, subjected to a very high strain rate, is loaded so rapidly in the axial direction that it will not be able to expand instantaneously in the lateral direction because of inertial restraint, thus producing an effective confining stress (Brace and Jones 1971; Bischoff and Perry 1991).

To study the behavior of materials at high strain rates, various experimental tests have been performed, such as the Charpy impact test, to determine the toughness of structural materials, or the well-known drop weight impact test (Gopalaratnam et al. 1996). Nevertheless, difficulties still remain in obtaining enough precision in the data sets when attempting to describe the behavior of concrete at high strain rates (>10^{2} s^{-1}). Recent improvements in data processing have shown that it was now possible to get good information via the split Hopkinson pressure bar (SHPB) (Gary and Zhao 1996). This device, which was initially designed to study the mechanical behavior of metals at high strain rates, has also been used to test concrete specimens because precise measurements of forces and displacements could be obtained.

In the present work, data available from SHPB unconfined compressive tests on concrete specimens (Gary 1990) will be used to study the dynamic behavior of concrete with a 3D numerical model based on a discrete-element method (DEM).

In this alternative numerical approach to more classical finite-element methods (FEM), the medium is considered to be fully discontinuous and a continuum is just a special case. These methods derived from molecular dynamics have already proven to be effective in dealing with complex media where continuous and discontinuous properties need to be handled concurrently, particularly in the case of dynamic loadings. Early applications of these methods and their advantages in the studies of high strain rate loadings have been seen when considering a shallow explosive event and the resulting wave propagation (Donzé et al. 1996), studying the evolution of the fracture patterns such as the radial fracture propagation from

[1]Assoc. Prof., Dept. of Earth Sci., GEOTOP, Univ. of Quebec at Montréal, C.P. 8888, Succ. Centre Ville, Montreal, PQ, Canada H3C 3P8. E-mail: fred@volcan.geotop.uqam.ca

[2]Res., Dept. of Earth Sci., GEOTOP, Univ. of Quebec at Montréal, C.P. 8888, Succ. Centre Ville, Montreal, PQ, Canada H3C 3P8. E-mail: sophie@volcan.geotop.uqam.ca

[3]Assoc. Prof., Laboratoire de Mécanique et Technologie, ENS de Cachan, Centre National de la Recherche Scientifique, Univ. Paris 6, 61, avenue du Président Wilson, 94235 Cachan cedex, France. E-mail: Laurent.Daudeville@lmt.enscachan.fr

[4]Res. Engr., DASE Laboratoire de Géophysique, Commissariat à l'Energie Atomique, B.P. 12, 91680 Bruyères le Châtel, France. E-mail: mariotti@ldg.bruyeres.cea.fr

[5]Assoc. Prof., Laboratoire de Mécanique et Technologie, ENS de Cachan, Centre National de la Recherche Scientifique, Univ. Paris 6, 61, avenue du Président Wilson, 94235 Cachan cedex, France. E-mail: Luc.Davenne@lmt.enscachan.fr

Note. Associate Editor: Gilles Pijaudier-Cabot. Discussion open until March 1, 2000. To extend the closing date one month, a written request must be filed with the ASCE Manager of Journals. The manuscript for this paper was submitted for review and possible publication on April 27, 1998. This paper is part of the ***Journal of Engineering Mechanics***, Vol. 125, No. 10, October, 1999. ©ASCE, ISSN 0733-9399/99/0010-1154–1163/$8.00 + $.50 per page. Paper No. 18239.

a blasthole (Donzé et al. 1997), or when characterizing the fragmentation process involved in a missile impacting a concrete beam (Magnier and Donzé 1998).

The DEM used to simulate a geomaterial such as concrete will be first presented followed by the methodology used to simulate the SHPB compressive tests. Unlike in 1D Malvern-Sokolovsky-type constitutive models where viscosity is required to explain the strain rate dependency (Zhao and Gary 1996), here in the 3D model the viscous terms are deliberately omitted to see if the sole presence of inertial effects can explain the data for strain rates on the order of 10^2 s^{-1}.

DEM

The present numerical method uses discrete spherical elements of individual radius and mass. These elements represent a polydisperse assembly with a size distribution obtained by using a growing technique described in Appendix I (Magnier et al. 1997). Once the assembly has been set, pairs of discrete elements are identified. This will be the first step in determining which elements are initially interacting. These interactions have been chosen to represent, as best as possible and in a simple way, the elastic and cohesive nature of a certain class of geomaterials such as concrete. To do this, elastic interaction forces with a tensile strength have been chosen. When this geomaterial is subjected to large deformations, the cohesive nature will disappear and fractures will propagate. To reproduce this fracturing process, a local rupture criterion is applied on the interaction forces. To account for the irreversibility of this process, all subsequent interactions will be noncohesive; that is, the tensile strength will be set to zero.

The numerical model solves the equations of motion with an algorithm similar to those used in molecular dynamics (Allen and Tildesley 1987) whereby the constitutive equations for each interaction are used to solve Newton's equations of motion. The explicit time integration of the laws of motion will provide the new displacement and velocity for each discrete element.

As time proceeds during the evolution of the system, large displacements of discrete elements may occur and new interactions may be created. One of the major parts of this numerical model will then be to determine the interacting neighbors of a given element. This will be done by defining an interaction range. Once this neighborhood is established, it is then necessary to identify all elements within it that are interacting. Depending on the spatial distribution of the discrete elements, two different methods are available to identify the interacting neighbors. If the distribution is rather compact with little fluctuation in size, a grid subdivision method is used (Allen and Tildesley 1987; Magnier et al. 1997). If, however, the distribution is dispersive with large-size fluctuations then the previous method will be costly, and a spatial sorting method is used (Müller 1996; O'Connor 1996; Magnier et al. 1997).

Constitutive Laws

The overall behavior of a material can be reproduced in this model by associating a simple constitutive law to each interaction. An interaction between elements a and b of radius R^a and R^b, respectively, is defined within an interaction range γ and does not necessarily imply that two elements are in contact. Then, these elements will interact if

$$\gamma(R^a + R^b) \geq D^{a,b} \tag{1}$$

where $D^{a,b}$ = distance between the centroids of elements a and b and $\gamma \geq 1$. This is an important difference from classical DEMs, which use spherical elements (Cundall and Strack 1979) where only contact interactions are considered ($\gamma = 1$). This choice was made so that the method could simulate materials other than simple granular materials, particularly those that involve a matrix as found in concretes. To account for the effects of this matrix, which may cement two aggregates that are not themselves in contact, the interaction range γ is set to be >1 when the assembly of elements is initially built. However, this long-range interaction is limited to nearest neighbors. Recall that the present assembly is made up of elements of different radii, which induces here a low number of initial contacts (see Appendix I).

A similar technique was used when simulating the propagation of fractures due to rock blasts (Donzé et al. 1997) or impacts (Magnier and Donzé 1998). It was seen to be of utter importance to obtain a proper localization of the fractures while using only contact interactions ($\gamma = 1$), the fractures were more diffuse.

The location of the interaction point is given by

$$\mathbf{x}^{a,b} = \mathbf{x}^a + (R^a - 0.5((R^a + R^b) - D^{a,b})\mathbf{n} \tag{2}$$

where $\mathbf{n}$ = unit vector pointing from element a to element b; and $\mathbf{x}^a$ = position vector of element a.

Interaction Forces

The interaction force vector $\mathbf{F}$ that represents the action of element a on element b may be decomposed into a normal and a shear vector $\mathbf{F}^n$ and $\mathbf{F}^s$, respectively, so that

$$\mathbf{F} = \mathbf{F}^n + \mathbf{F}^s \tag{3}$$

The normal force vector may be expressed such that it accounts for possible irreversible deformations. However, this irreversibility will only be initiated after a compressional phase ($D^{a,b} < D^{a,b}_{eq}$, where $D^{a,b}_{eq}$ is the equilibrium distance between the two elements a and b, which was set when the interaction was created). In that case, a different loading and unloading path can be considered. Loading means that $|\mathbf{F}^n|$ is increasing, whereas unloading means that it is decreasing. The normal force vector after a compressional phase can then be written (Walton 1993)

$$\mathbf{F}^n = \begin{cases} K^n(D^{a,b}_{eq} - D^{a,b})\mathbf{n} & \text{for loading} \\ \alpha K^n(D^{a,b}_{eq} - D^{a,b} - D^{a,b}_{\text{correction}})\mathbf{n} & \text{for unloading} \end{cases} \tag{4}$$

where $D^{a,b}_{\text{correction}}$ represents the correction to be applied on the equilibrium distance so that the absolute value of the unloading force is always less than or equal to the absolute value of the loading force. The value of α must be ≥ 1. Note that for $\alpha = 1$, $D^{a,b}_{\text{correction}} = 0$ and for $\alpha \to \infty$, $D^{a,b}_{\text{correction}} \to (D^{a,b}_{eq} - D^{a,b})$.

After each unloading path, the equilibrium position is updated such that

$$(D^{a,b}_{eq})_{\text{new}} = (D^{a,b}_{eq})_{\text{old}} - D^{a,b}_{\text{correction}} \tag{5}$$

For the case where compression has never occurred and where only tension ($D^{a,b} < D^{a,b}_{eq}$) is involved, the loading and unloading paths are the same, and the normal force vector may be exposed as

$$\mathbf{F}^n = K^n(D^{a,b}_{eq} - D^{a,b})\mathbf{n} \tag{6}$$

Fig. 1 summarizes the behavior of the normal force. As long as $F^n \geq F^n_{\max}$ the normal force follows the solid line.

The normal stiffness K^n is linear, and it is expressed assuming that the stiffnesses k^a_n and k^b_n of the interacting elements act in series (within a constant) so that

$$K^n = 2\left[\frac{k^a_n k^b_n}{k^a_n + k^b_n}\right] \tag{7}$$

The shear vector force $\mathbf{F}^s$ is computed incrementally and was given by other authors (Hart et al. 1988; *PFC3D* 1995).

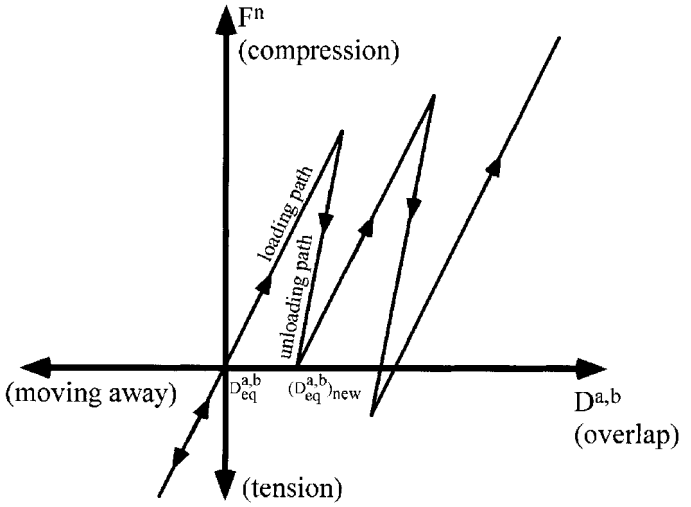

FIG. 1. Behavior of Normal Component of Interaction Force. Slope of Loading Path during Compression Is K^n; It Is αK^n for Unloading Path during Compression

It is computed in two steps. First it is updated with respect to the possible rotations that occur between times $t - 1$ and t. The first rotation is with respect to the change in normal directions of the interaction and can be expressed as

$$\mathbf{F}^s_{rot.1} = \mathbf{F}^s_{t-1} - \mathbf{F}^s_{t-1} \times \mathbf{n}_{t-1} \wedge \mathbf{n}_t \tag{8}$$

whereas the second rotation is the relative rotation of the elements about the new normal direction

$$\mathbf{F}^s_{rot.2} = \mathbf{F}^s_{rot.1} - \mathbf{F}^s_{rot.1} \times \overline{\boldsymbol{\omega}} \Delta t \tag{9}$$

where $\overline{\boldsymbol{\omega}}$ = average angular velocity vector of the two interacting elements about the new normal direction; and Δt = time step.

The second step consists of computing the incremental vector itself given by

$$\Delta \mathbf{F}^s = -K^s \Delta \mathbf{U}^s \tag{10}$$

where $\Delta \mathbf{U}^s$ is the shear displacement vector increment between the locations of the interacting points of the two elements over a time step Δt. The shear stiffness K^s is linear, and it is expressed assuming that the stiffness k_s^a and k_s^b of the interacting elements act in series (within a constant) so that

$$K^s = 2 \left[\frac{k_s^a k_s^b}{k_s^a + k_s^b} \right] \tag{11}$$

Finally, the new shear interaction force can be expressed as

$$\mathbf{F}^s = \mathbf{F}^s_{rot.2} + \Delta \mathbf{F}^s \tag{12}$$

The total interaction force vector $\mathbf{F}$ can also be written $\mathbf{F}^{a,k}$ for the interaction between elements a and b if this interaction is the kth interaction for element a. Once it has been calculated, all other interactions that element a has with other elements are now considered, and the resulting interaction forces are computed. Then, the total force acting on element a is the sum of all n interaction forces and all other l applied forces (gravity, boundary conditions, etc.) such that

$$\mathbf{F}^a = (-1) \left(\sum_{k=1}^{n} \mathbf{F}^{a,k} \right) + \sum_{j=1}^{l} \mathbf{F}^j \tag{13}$$

The total moment acting on element a is

$$\mathbf{M}^a = (-1) \left(\sum_{k=1}^{n} [(\mathbf{x}^{a,k} - \mathbf{x}^a) \times \mathbf{F}^k] \right) \tag{14}$$

Strength Properties

The brittle properties of the medium can then be introduced if both a normal and shear rupture threshold are defined for the corresponding interaction force. This is a Mohr-Coulomb rupture criterion. Beyond these thresholds the nature of the interaction force changes. Thus, for a given interaction, a maximum tensile strength T (with $T > 0$) is given and a maximum normal force $F^n_{\max}$ is defined such that

$$F^n_{\max} = -T\tilde{A}_{int} \tag{15}$$

where $\tilde{A}_{int}$ = average surface where the interaction is defined with

$$\tilde{A}_{int} = \pi \left(\frac{R^a + R^b}{2} \right)^2 \tag{16}$$

A maximum interaction distance $D_{\max}$ is defined such that

$$D_{\max} = D_{eq} + (\beta + 1) \left(\frac{|F^n_{\max}|}{K^n} \right) \tag{17}$$

where D_{eq} = equilibrium distance; and β = softening factor for this interaction with $\beta > 0$. Note that in all of these developments, the indices a and b, which represented the interacting elements, have been dropped to lighten the formulations. If

$$F^n < F^n_{\max}; \quad D \geq D_{\max} \Rightarrow \begin{cases} F^n = 0 \\ F^s = 0 \end{cases} \tag{18a,b}$$

and if

$$F^n < F^n_{\max}; \quad D < D_{\max} \Rightarrow F^n = \frac{K^n}{\beta} (D - D_{\max}) \tag{19a,b}$$

Fig. 2 summarizes the behavior of the normal force for two different values of β that illustrates the difference between a brittle elastic behavior (dotted line) and a quasi-brittle behavior [i.e., presence of softening (dashed line)]. As long as $F^n \geq F^n_{\max}$ the normal force follows the solid line. As soon as $F^n < F^n_{\max}$ and depending on the value chosen for β, different paths can be followed. If $\beta \to 0$ then $D_{\max} \to D_{\max 1}$ and rupture occurs (dotted line). If $\beta = 2$ then $D_{\max} = D_{\max 2}$, and before rupture the normal force follows the dashed line.

However, a global softening may still be induced at the macroscopic scale, whereas the local softening factor tends to zero if the size distribution of the elements is large enough. Thus, if there is a large distribution of radii for the elements, according to (15) there will then be a large distribution of maximum normal forces that will in turn introduce softening effects (Herrmann et al. 1989). Therefore, some caution must be exercised before using a local softening factor.

The maximum shear force can be calculated as

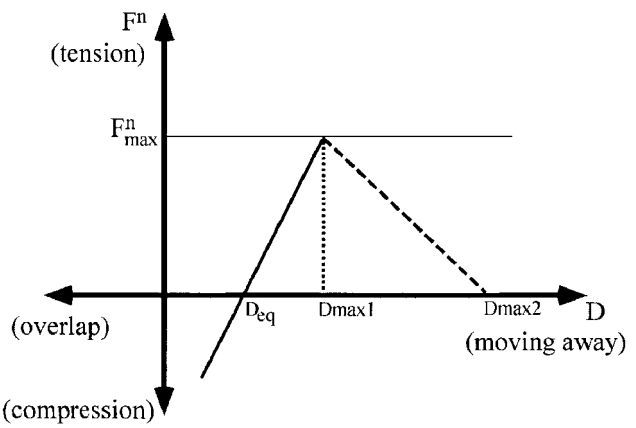

FIG. 2. Strength Properties of Normal Force

$$F^s_{\max} = c\tilde{A}_{int} + F^n \tan \phi \tag{20}$$

where c = cohesion; and ϕ = friction angle. If the absolute value of the shear force is

$$|F^s| = (\mathbf{F}^s \cdot \mathbf{F}^s)^{1/2} \tag{21}$$

which is greater than $|F^s_{\max}|$, then the shear force is reduced to the limiting value and written as follows:

$$\mathbf{F}^s_{\text{reduced}} = \mathbf{F}^s[F^s_{\max}/|F^s|] \tag{22}$$

Law of Motion

Newton's laws of motion are used. To obtain the acceleration $\ddot{\mathbf{x}}$ of the ith element from the total unbalanced force $\mathbf{F}$ applied on it

$$m\ddot{\mathbf{x}} = \mathbf{F} \tag{23}$$

where m = mass of the element. The equation for rotational motion can be written as follows:

$$\mathbf{M} = \dot{\mathbf{H}} \tag{24}$$

where $\dot{\mathbf{H}}$ = angular momentum of the ith element; and $\mathbf{M}$ = resultant moment acting on this element, which may also be written for spherical elements as follows:

$$\mathbf{M} = I\dot{\boldsymbol{\omega}} = \left(\frac{2}{5} mR^2\right) \dot{\boldsymbol{\omega}} \tag{25}$$

where I = moment of inertia for the ith element; $\dot{\boldsymbol{\omega}}$ = its angular acceleration vector; and R = its radius.

Explicit integration of Newton's equations for both translational and rotational motion is done by the basic ''leapfrog'' method (Allen and Tildesley 1987). The finite-difference equation for the velocity of an element is given by

$$\dot{\mathbf{x}}^{(t+\Delta t/2)} = \dot{\mathbf{x}}^{(t-\Delta t/2)} + \frac{\mathbf{F}^{(t)}}{m} \Delta t \tag{26}$$

from which the displacement is obtained

$$\mathbf{x}^{(t+\Delta t)} = \mathbf{x}^{(t)} + \dot{\mathbf{x}}^{(t+\Delta t/2)} \Delta t \tag{27}$$

and the angular velocity is given by

$$\boldsymbol{\omega}^{(t+\Delta t/2)} = \boldsymbol{\omega}^{(t-\Delta t/2)} + \frac{\mathbf{M}^{(t)}}{I} \Delta t \tag{28}$$

where t refers to the current time step; and Δt = time step.

Macroscopic Calibration of Elastic and Strength Properties

The calibration procedure of the model requires that the macroscopic constitutives laws of the material be derived from both its microscopic behavior. In the present model, the material is assimilated to a set of discrete elements for which the macroscopic elastic properties, denoted here as Poisson's ratio ν and Young's modulus E, are defined in terms of the local stiffnesses. To determine these elastic properties, numerical compressional tests have been run, and the values linking Poisson's ratio ν and Young's modulus E to the dimensionless values of K^s/K^n were obtained. Relations fitting these values can be expressed as

$$E = \frac{\bar{D}_{eq}}{\tilde{A}_{int}} K^n \left(\frac{0.825K^n + 2.65K^s}{2.5K^n + K^s}\right) \tag{29}$$

where $\bar{D}_{eq}$ = average distance between two discrete elements; $\tilde{A}_{int}$ = its associated average interaction surface; and

$$\nu = \frac{K^n - K^s}{2.5K^n + K^s} \tag{30}$$

The corresponding numerical curves are shown in Fig. 3. The dashed line corresponds to the Voigt model, the dot-dashed line to the best-fit model (Liao et al. 1997), and the solid line is the estimated relation fitting the numerical values, which are represented by circles. Given the macroscopic values for the concrete samples used in the experimental procedure (Toutlemonde 1995), the local parameters K^n and K^s are determined. Once these continuous properties are obtained, the strength properties are then calibrated. To do this, uniaxial strain tests are performed in both compression and tension until the model reproduces rupture thresholds found in the experimental static case (Toutlemonde 1995). A good agreement is found between the behavior of the discrete-element model and that of samples in static experiments (Camborde et al. 1997).

SHPB EXPERIMENT

A typical SHPB experimental setup (Zhao and Gary 1996) can be seen in Fig. 4. It consists of two long aligned metallic bars and a short concrete specimen between them. A projectile impacts the free end of the input bar thus leading to the development of a compressive longitudinal incident wave $\varepsilon_i(t)$. Once it arrives at the bar-specimen interface, it splits into a

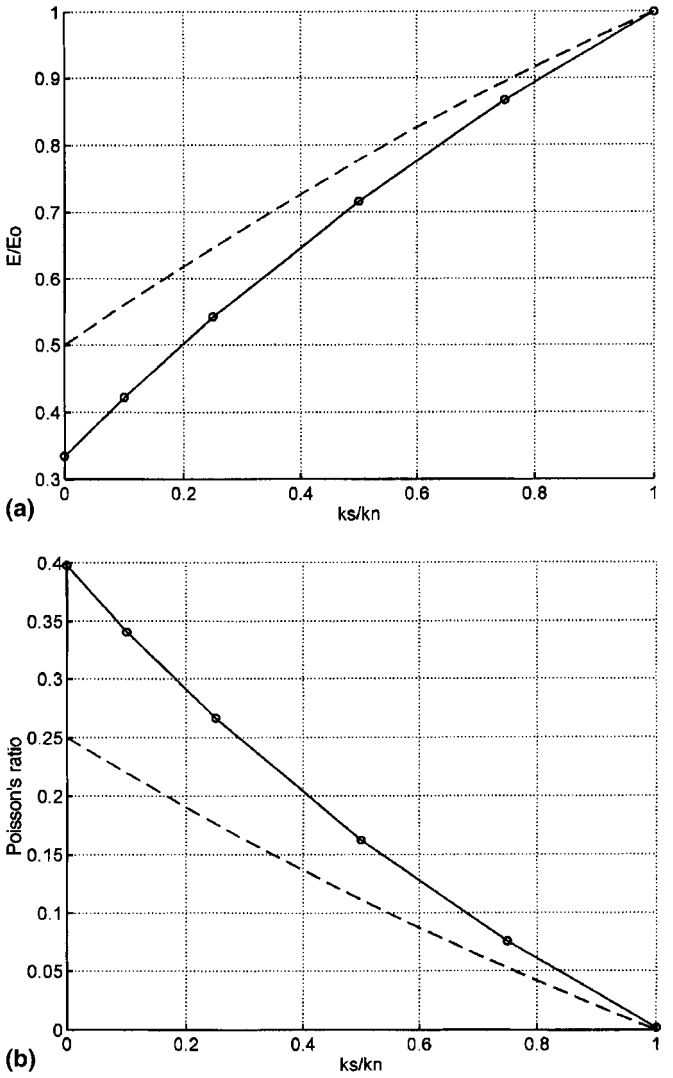

FIG. 3. Functions of Stiffnesses Ratio K^s/K^n: (a) Young's Modulus; (b) Poisson's Ratio

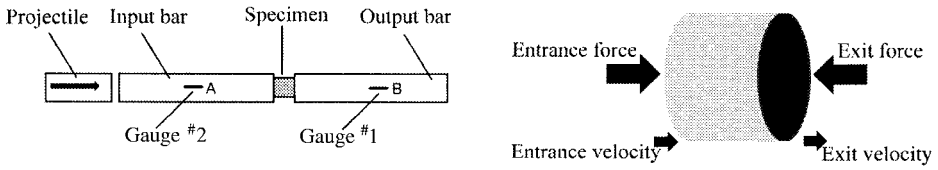

FIG. 4. Setup for SHPB Experiment

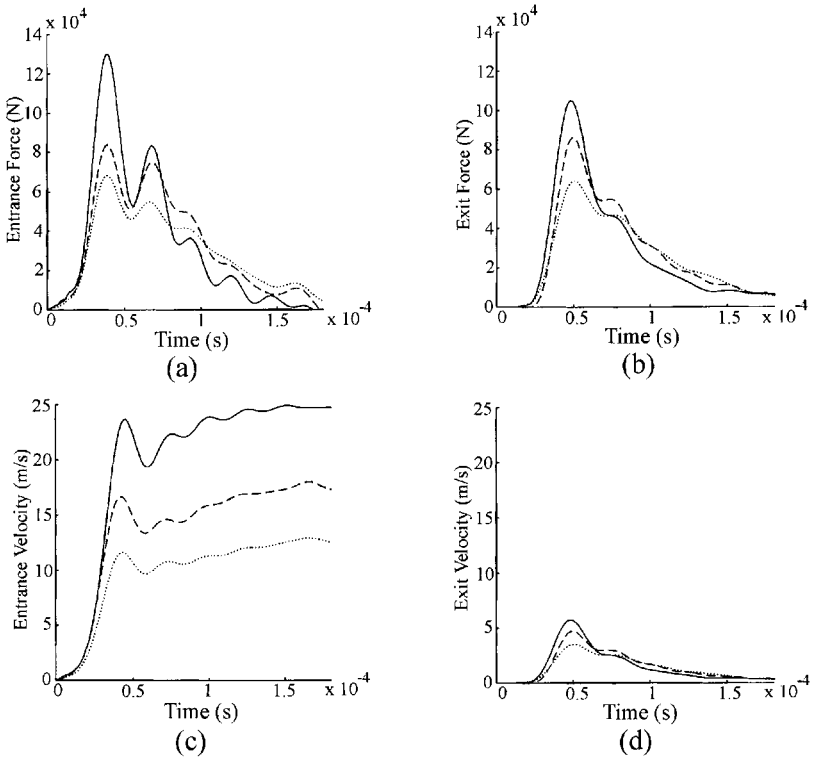

FIG. 5. Measured Experimental Data. Solid, Dashed, and Dotted Lines Are, Respectively, Experiments ms5b (700 s^{-1}), ms3b (500 s^{-1}), and ms2b (350 s^{-1})

reflected wave $\varepsilon_r(t)$, which travels in the input bar, and a transmitted wave $\varepsilon_t(t)$, which travels in the output bar. These three waves are recorded by gauges that have been cemented on each bar. They are then artificially shifted to record them at the bar-specimen interfaces, so that the forces and velocities measured on both faces of the specimen (Gary and Zhao 1996) are given by

$$V_{\text{entrance}}(t) = C(\varepsilon_i(t) - \varepsilon_r(t)) \tag{31}$$

$$V_{\text{exit}}(t) = C\varepsilon_t(t) \tag{32}$$

$$F_{\text{entrance}}(t) = S_B E(\varepsilon_i(t) + \varepsilon_r(t)) \tag{33}$$

$$F_{\text{exit}}(t) = S_B E\varepsilon_t(t) \tag{34}$$

where $C = \sqrt{E/\rho}$ = celerity of the medium; E = Young's modulus; ρ = density; and S_B = cross-sectional area of the bars.

Once these forces and velocities are obtained, a so-called three-waves formula (Lindholm 1964) gives the average strain rate and the average stress imposed on the specimen, so that

$$\dot{\varepsilon}_s(t) = \frac{V_{\text{exit}}(t) - V_{\text{entrance}}(t)}{l_s} \tag{35}$$

$$\sigma_s(t) = \frac{F_{\text{entrance}}(t) + F_{\text{exit}}(t)}{2S_s} \tag{36}$$

where l_s and S_s denote, respectively, the length and the cross-sectional area of the specimen.

The complete data set then consists of F_{entrance}, F_{exit}, V_{entrance}, and V_{exit}. If the correct constitutive behavior has been used in a model, then given one of these pairs, the other data pair should be obtained. In the following simulations the velocities will be used as the input data, and the forces will thus be computed numerically and compared with the real experimental data forces.

Experimental Data Set

SHPB tests on concrete specimens have been carried out by Gary (1990) in the framework of the ''GRECO géomatériaux project,'' and data obtained from these different tests were made widely available. The data set, after the applied time shift and corrected to be representative of data gathered at the bar-specimen interface, is shown in Fig. 5.

The concrete specimens that are used are cylinders with a height of 0.036 m and a diameter of 0.036 m. The density is 2,500 kg/m^3, and the average compressive wave velocity is 3,865 m/s (Toutlemonde 1995).

Three loading experiments, ms2b, ms3b, and ms5b at 350, 500, and 700 s^{-1} strain rates, respectively, have been run; for each of these runs both the entrance and exit velocities and forces are plotted. The first thing that can be noted on these curves is that the behavior is quite different for each loading rate experiment. In particular, it can be seen that the primary exit force peaks [Fig. 6(b)] in experiments ms2b and ms5b are less than the primary entrance force peaks [Fig. 5(a)], whereas in experiment ms3b it is the opposite case. This difference does not seem to be representative of the loading rate. This might be due to variable experimental conditions such as boundary conditions or specimen material properties.

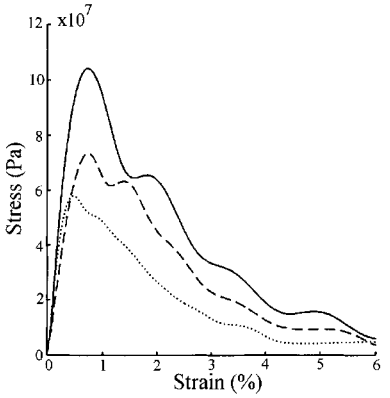

FIG. 6. Stress versus Strain Curves for Experimental Data Set. Solid, Dashed, and Dotted Lines Are, Respectively, Experiments ms5b (700 s^{-1}), ms3b (500 s^{-1}), and ms2b (350 s^{-1}). Slopes of Curves Give Elastic Modulus

TABLE 1. Local Interaction Parameters

Parameter (1)	Initial interactions (2)	Contact interactions (3)
γ	1.4	1.0
α	1	2
β	1	10^{-5}
T (MPa)	4	0
ϕ (degrees)	17	40
K^s/K^n	0.4	0.4
K^n	Depends on size and interactions [see Eqs. (29) and (30)]	

The arrival times of the exit force and velocities as shown in Figs. 5(b and d), respectively; and discussed next. The measured time delays between the entrance and exit signals range from 10 μs for experiment ms3b and 7 μs for experiment ms5b. This 3-μs difference in travel time in a medium with an average compressive wave velocity of 3,865 m/s represents a difference in specimen length of more than 30%.

The dynamic Young's moduli for these experiments are measured to range from 14.0 GPa for experiment ms3b to 25 GPa for experiment ms5b as obtained from the slopes of the stress strain curves of Fig. 6. These moduli are much lower than what was expected from the static value (Toutlemonde 1995), which is more than 30 GPa.

Such fluctuations in the data set are not surprising when considering the very high strain rates at which these experiments are run and may come from the error bar on the applied correction of the travel times of the compressive waves (Gary, personal communication, 1997) but it makes it difficult to define a precise reference material that could be used in the numerical model. In the numerical model, the density and the strength properties are kept as given by the laboratory experiments, but Young's moduli are modified so that the waveforms and amplitudes of the entrance and exit forces that are computed fit those that are observed.

NUMERICAL SETUP

Up to 2×10^4 spherical discrete elements with sizes ranging from 5×10^{-4} to 5×10^{-3} m have been used to build the numerical concrete sample. These have been distributed spatially with the growing technique described in Appendix I.

Two different interaction types have been defined between elements: (1) The initial interactions, before any deformation occurs, are defined to reproduce both the cohesive and brittle-elastic nature of the concrete sample; and (2) following the possible ruptures of the initial interactions during the deformation process, new contact interactions may occur but with no tensile resistance or cohesion. They are strictly frictional interactions. Specific parameters for the two kinds of interactions are given in Table 1.

Different values of α introduced in (4) were used for the contact interactions. This factor is used to account for the effect of compaction when the material undergoes fragmentation. Note, that this parameter may be associated to a local restitution coefficient given by $e = \sqrt{1/\alpha}$, which is independent of the relative velocity of impact (Walton 1993). The values of T and ϕ for the initial interactions were chosen such that for the size distribution of the discrete elements and for the value of $\gamma = 1.4$ the macroscopic values of the tensile strength is about 5 MPa and the internal friction angle is about 40°.

In Fig. 6, the slope for experiment ms2b (350 s^{-1}) and ms5b (700 s^{-1}) is the same whereas it differs for experiment ms3b (500 s^{-1}), which implies that the latter has a lower elastic modulus. It is measured to be 0.625 times that of experiments ms2b and ms5b. This ratio was kept for the elastic moduli of the numerical simulations where the normal local stiffness K^n used in the model of ms3b is 0.625 times that of ms2b and ms5b.

The experimental entrance velocity is applied to the elements that make up the entrance surface of the numerical concrete specimen, and the experimental exit velocity is applied to the elements that make up its exit surface. The radial displacement values are assumed to be zero on the entrance and exit surfaces. The resulting entrance force is computed by summing all the forces applied on the elements that make up the entrance surface, and the resulting exit force is the sum of all the forces applied on the elements that make up the exit surface. Given the experimental velocity histories, at each time step the applied entrance and exit velocities are updated leading to the computation of numerical force histories.

NUMERICAL RESULTS

The computed numerical force histories for the experiments at 350, 500, and 700 s^{-1} are plotted in Fig. 7. To compare them with the experimental curves, the latter have also been plotted for each individual strain rate.

Clearly, the numerical results fit the experimental results quite well during the first 100 μs. In particular, the signal waveform is satisfactorily reproduced during most of this time. The amplitudes also fit well except in the case of experiment ms5b (700 s^{-1}) where the numerical exit force is greater than the experimental record. However, by looking at Fig. 5, note that the amplitude ratio between experiments ms3b and ms2b is 1.23 for a strain rate difference of 150 s^{-1}, whereas between experiments ms5b and ms3b this ratio goes to 1.55 for a strain rate difference of 200 s^{-1}. Yet, in the exit signals, the ratios are now 1.35 and 1.20, when it was expected that the second ratio would be higher than the first as it is in the entrance signals. On the other hand, in the numerical results of Fig. 7 the exit ratios are 1.34 and 1.44, where the second ratio is indeed greater than the first as expected. Thus, a question remains on the recording precision in experiment ms5b.

Beyond the first 100 μs, however, the amplitudes of the experimental data and the numerical simulations start to diverge, reflecting a more brittle behavior in the numerical experiment than in the real data set as shown in Fig. 8. This might be due to the distribution of the sizes of the elements used in the present simulation.

Fig. 9 shows that the distribution interval is rather narrow unlike the size distribution of aggregates in concrete (Schlangen 1993). This means that the distribution interval of the rupture thresholds will in turn be narrow as it depends directly on the distribution of the radii as seen in (15) and (16). It is known that as the distribution interval of rupture thresholds

narrows the more important it is that the post-peak drop tends toward a catastrophic regime (Herrmann et al. 1989). Therefore, to obtain a better fit during the postpeak sequence (i.e., to have a more ductile behavior), a wider distribution would be required. In the present numerical simulation the use of the softening factor β introduced in (17) slightly overcomes the noted divergence in the postpeak behavior by making the material a little more ductile. Nonetheless, it should become obsolete if a better size distribution of elements was used. Finally, the introduction of different values of α in (4) had little effect on the postpeak fit in the absence of confinement, as is the case here.

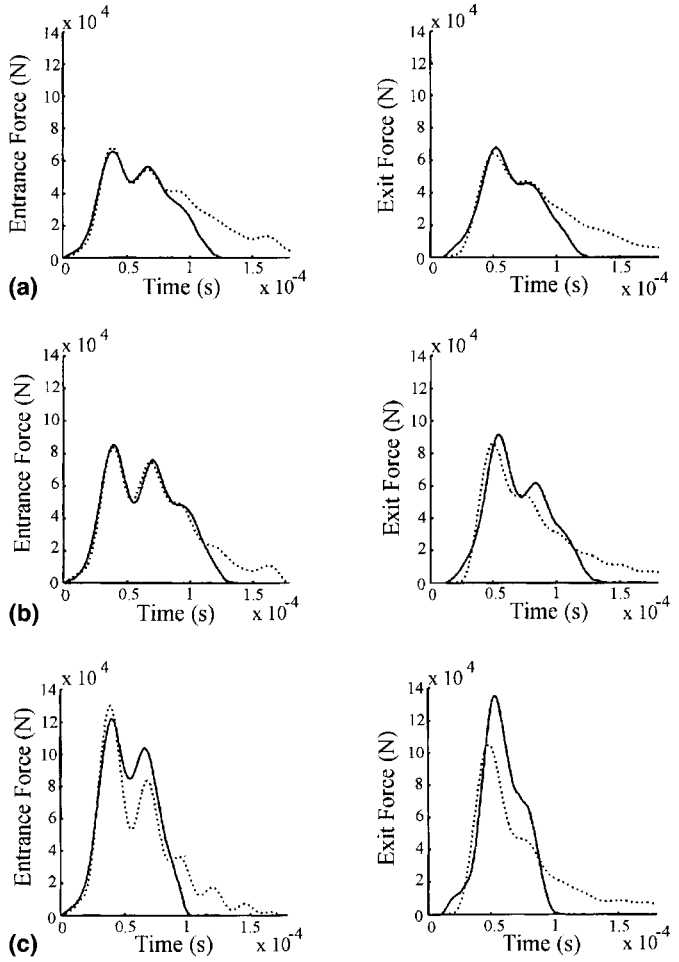

FIG. 7. Two Plots for Strain Rate Deformations of: (a) 350 s^{-1}; (b) 500 s^{-1}; (c) 700 s^{-1}. Dotted Lines Are Original Experimental Curves; Solid Lines Are Computed Numerical Results

DISCUSSION

Given that these numerical results seem satisfactory, the question is then what happens in the physical model to explain these results? One hypothesis that was proposed (Gopalaratnam 1996) was that the strain rate dependency could be explained by a viscoelastic behavior of the cement paste. However, in the present numerical model viscous terms were deliberately omitted, yet the numerical data fit the real data. Thus, in this model, an inertia based hypothesis (Janach 1976; Bischoff and Perry 1991, 1995) might explain the strain rate dependency. This inertial effect should imply that for a given average stress as defined in (36), for different strain rates, the extent of the damage will differ. Locally, the inertial effects will tend to oppose the opening of cracks, and the time available for microcrack development depends on the loading time. It should be seen that the higher the strain rate, the smaller the propagation distance of the damage area. To see if this is the case here, for a given average stress of 50 MPa, lengthwise and radial cuts are made through the center of the specimen for two strain rates of 350 and 700 s^{-1}. The state of the damage is shown in Fig. 10 where the discrete elements have been colored as a function of the ratio between the number of rupture interactions and the number of initial cohesive interactions. As the damage increases, the color darkens. V_{in} is the entrance velocity, and V_{out} is the exit velocity. These velocities are applied on the elements that have been joined by a black line.

It is indeed seen that as the strain rate increases, the extent of the damage lessens. It is noteworthy that this damage is not homogeneous and tends to propagate inwardly from the lateral free surfaces of the specimen thus forming a contact cone as seen in real experiments (Janach 1976). Unlike quasi-static experiments where fracturing is well localized into narrow shear zones (Lockner and Moore 1992), here the damage area is more diffuse, and the resilient contact cone is bigger on the impact side. The damage pattern is comparable to the theoretical pattern proposed by Janach (1976), and the proposed unloading process for SHPB tests is given in Fig. 11.

An explanation is that the compressive stress wave C in the brittle material generates a dilation in the radial direction because of the opening of cracks. Thus, the material exhibits a reduced unloading modulus in the radial direction that allows the damage zone to propagate inwardly from the free surface with an unloading velocity C_f, which can be less than the compressive wave velocity. If this is the case, then the unloading could be sufficiently slow so that the central core of the specimen would not have had time to unload, which means that this specimen will have a greater load-carrying capacity (Bischoff and Perry 1991). Consequently, if the displacement field is plotted as in Fig. 12, there should be a larger displacement where the unloading has already occurred that is near the lat-

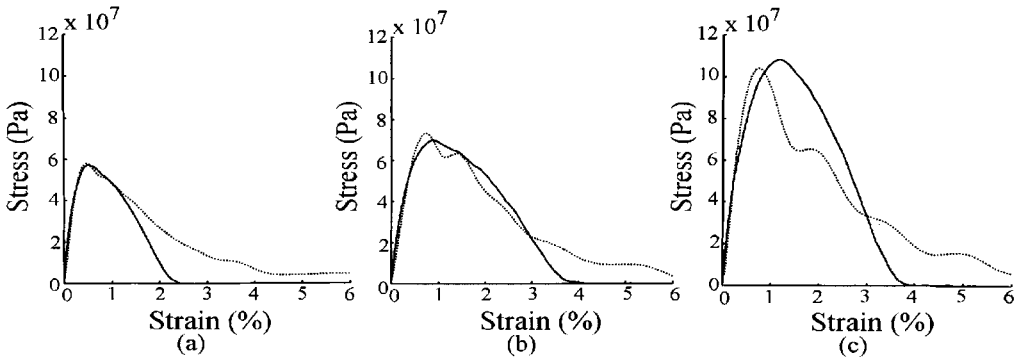

FIG. 8. (a) 350 s^{-1}; (b) 500 s^{-1}; (c) 700 s^{-1}. Dotted Lines Are Experimental Curves; Solid Lines Are Numerical Curves

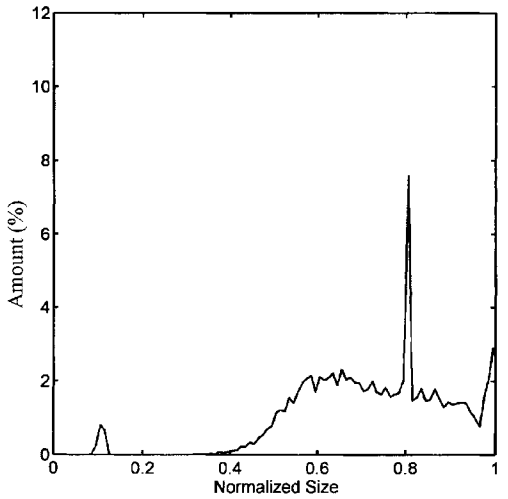

FIG. 9. Distribution of Radius Size for Discrete Elements. Elements' Sizes Vary between 5×10^{-4} and 5×10^{-3} m

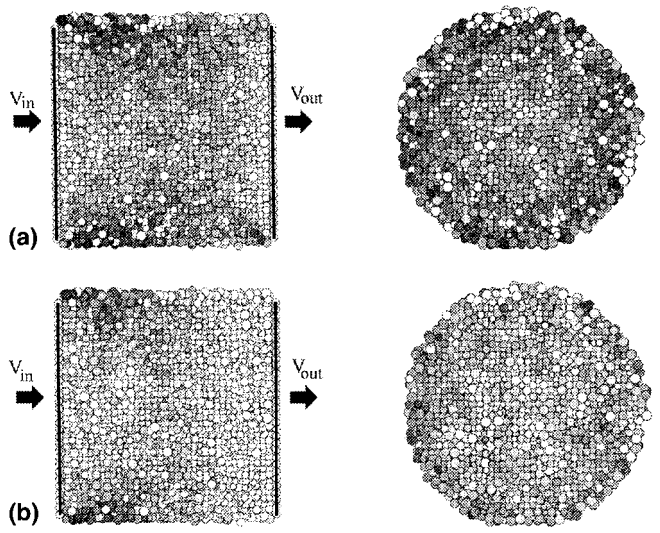

FIG. 10. Damage Taken at Loading of 50 MPa for: (a) 350 s^{-1}; (b) 700 s^{-1}. Left Views Are Axial Cuts; Right Views Are Radial Cuts through Center of Specimen

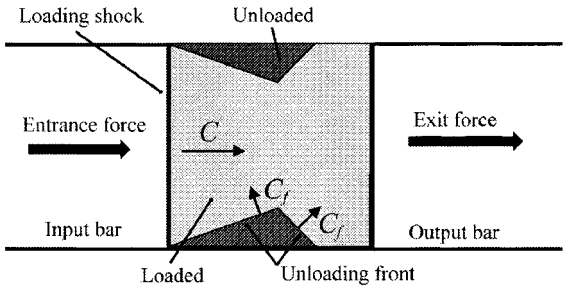

FIG. 11. Simplified Lateral Unloading Process Proposed for Cylindrical Specimen that Fails by Brittle Fracture in SHPB Compressional Tests

eral free surfaces [Fig. 12(a), right view]. By increasing the strain rate, the unloading will have had even less time, and the displacement near the lateral free surfaces will tend to be smaller [Fig. 12(b); right view]. As the unloading is even less, the load-carrying capacity is increased thus leading to an apparent strain rate effect. This can be considered as a lateral inertial confinement effect. Moreover, as observed on the left-hand side of Figs. 12(a and b), the displacement in the axial direction also decreases with an increasing strain rate that suggests that the axial inertial effect is not negligible when considering the increased strength of the specimen.

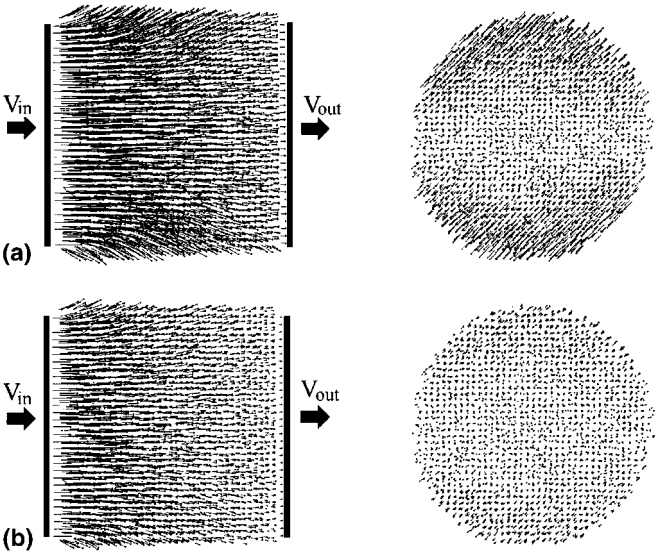

FIG. 12. Displacement Fields for: (a) 350 s^{-1}; (b) 700 s^{-1}. Arrows Represents Displacement between Time $t = 0$ and Time when Loading Is 50 MPa. Left Views Are Axial Cuts; Right Views Are Radial Cuts through Center of Specimen

Based on these results, the inertia hypothesis can explain the strain rate dependency.

CONCLUSIONS

This numerical experiment has shown an increase in compressive strength with increasing loading rates as observed in the experimental data set. A good fit between the experimental and the numerical data was obtained without requiring the use of viscosity in the model. However, the postpeak behavior of the numerical experiment did not adequately fit the experimental data. A more ductile behavior would be required that could be obtained by modifying the numerical model's discretization. A better distribution interval of the elements' sizes should be used.

Nonetheless, the general behavior of concrete at high strain rate compressions can be characterized. In particular, the strain rate dependency could be attributed to inertial effects with this kind of model. These inertial effects implied that for a given average stress, for different strain rates, the extent of the damage differed. The higher the strain rate, the less the damage zone spread. This damage was not homogeneous and tended to propagate inwardly from the lateral free surfaces of the specimen thus forming a contact cone. By plotting the displacement fields, a larger displacement was observed where the unloading had already occurred. The load-carrying capacity was increased thus leading to an apparent strain rate effect that could be considered as a lateral inertial confinement effect.

New insights into the problem were gained by being able to have access to both macroscopic information such as stress and strain levels and local information such as the displacement and rupture of the aggregates. This was made possible by using a micromechanic model based on the DEM, which is well adapted in the field of deformations at high strain rate where continuous media undergo fragmentation.

APPENDIX I. GROWING TECHNIQUE

The aim of the growing technique is to be able to generate a compact set of discrete elements of various sizes in a 3D volume of arbitrary geometry. To do this a number of steps are required.

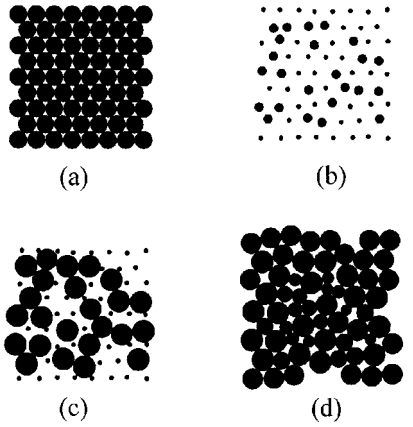

FIG. 13. Growing Technique for Discrete Elements

First, an initial set of elements, all of identical radius R_{init}, are distributed according to the most compact geometry possible [e.g., a face centered cubic lattice for the 3D problem (triangular for 2D) as represented in Fig. 13(a)].

The second step is to redistribute the radii of the elements according to two sizes such that $R_{\min} < R_{\max} < R_{init}$ with $R_{\min} = \delta_1 R_{init}$ and $R_{\max} = \delta_2 R_{init}$, where $\delta_1 < \delta_2 < 1$.

A random pick ξ is made between [0, 1] for each element a such that

$$\text{if } \begin{cases} 1 - \xi^n \geq \Theta \Rightarrow R^a = R_{\max} \\ 1 - \xi^n < \Theta \Rightarrow R^a = R_{\min} \end{cases} \tag{37}$$

with $n \geq 0$ and $\Theta < 1$, which are introduced to adjust the amount of disorder wanted. n and Θ are chosen for the entire set of discrete elements.

The initial positions of the elements are slightly modified in a random manner while avoiding the overlap of elements so that the new modified position of element a is

$$x^a_{mod} = x^a + \frac{\varepsilon R^a}{\sqrt{2}} (2\zeta^a - 1) \quad \text{with} \quad \zeta^a \in [0, 1] \tag{38}$$

where ζ^a is randomly selected; and ε = amplitude of the perturbation. For $n = 1$ and $\Theta = 0.6$, Fig. 13(b) is obtained with $\delta_1 = 0.25$ and $\delta_2 = 0.5$.

After this disorder is introduced, the elements are not in contact. To obtain the most compact distribution, the voids need to be filled as much as possible. To do this, the elements are allowed to grow in two steps. First, all elements of size $R_{\max}$ are allowed to grow, and all elements of size $R_{\min}$ are kept at a fixed position and size. The growth increment is the same at each growth iteration. The elements continue to increase in size until either a predefined maximum allowable size is reached or a predefined maximum element overlap is attained. In general, this latter criterion is limited to a few percent of the radius. Then, if an overlap is present, the radii of the two elements are decreased to the point where the elements are only in contact. Once all these elements have reached either one of these thresholds, as shown in Fig. 13(c), they are not allowed to move while the second growth step begins. During this step, all elements of size $R^a = R_{\min}$ will start to grow. As in the preceding step, these elements will grow until they reach one of two thresholds: (1) The maximum allowable radius, which is less than the maximum allowable radius of the first growth step; or (2) the maximum overlap, which is also less than the maximum overlap of the previous step. Once again, in the case of an overlap, the radii of the concerned elements are reduced until the overlap disappears. This final growth step is illustrated in Fig. 13(d). With this method, for a 2D problem, there will be an average of three contacts between discrete elements and six contacts for a 3D problem. In all cases there will always be a minimum of one contact.

This means that to have approximately the same number of interactions as an element would have with its nearest neighbors, if distributed according to the most compact lattice (e.g., 12 in a face centered cubic), additional interactions will need to be defined. Thus, long-range interactions are used between elements in the model.

An alternative way to increase the number of contacts between elements would be to introduce smaller-size elements in the remaining voids. This would increase the computational time.

The disadvantage of this method is that it is still difficult to adequately control the static distribution of the discrete elements' sizes. The advantages, on the other hand, are that 3D space is well occupied whatever the complexity of the macrostructure with enough disorder that anisotropic preferential fracturing is avoided.

ACKNOWLEDGMENTS

The present work was undertaken while one of the first writers was an invited professor at the Laboratoire de Mécanique et Technologie, Paris. Funding for this study was provided in part by the Laboratoire de Détection et Géophysique-Commissariat à l'Énergie Atomique. The writers would also like to thank two anonymous reviewers for their helpful comments.

APPENDIX II. REFERENCES

Allen, M. P., and Tildesley, D. J. (1987). *Computer simulation of liquids*. Clarendon, Oxford, England.

Bischoff, P. H., and Perry, S. H. (1991). ''Compressive behaviour of concrete at high strain rates.'' *Mat. and Struct.*, 24, 425–450.

Bischoff, P. H., and Perry, S. H. (1995). ''Impact behavior of plain concrete loaded in uniaxial compression.'' *J. Engrg. Mech.*, ASCE, 121(6), 685–693.

Brace, W. F., and Jones, A. H. (1971). ''Comparison of uniaxial deformation in shock and static loading of three rocks.'' *J. Geophys. Res.*, 76, 4913–4921.

Camborde, F., Mariotti, C., and Donzé, F. (1997). ''Application de la méthode des éléments discrets à la modélisatiob du béton sous chargement statique.'' *Proc., GEO '97*, GEO Publisher, Aussois, France (in French).

Cundall, P. A., and Strack, O. D. L. (1979). ''A discrete numerical model for granular assemblies.'' *Géotechnique*, London, 29, 47–65.

Curbach, M., and Eibl, J. (1989). ''Nonlinear behaviour of concrete under high compressive loading rates.'' *Proc., Int. Conf. on Recent Devel. in Fracture of Concrete and Rock*, Elsevier Science, New York.

Donzé, F., Bouchez, J., and Magnier, S. A. (1997). ''Modeling fractures in rock blasting.'' *Int. J. Rock Mech.*, 34, 1153–1163.

Donzé, F., Magnier, S. A., and Bouchez, J. (1996). ''Numerical modeling of a highly explosive source.'' *J. Geophys. Res.*, 101, 3103–3110.

Gary, G. (1990). *Essais à grande vitesse sur béton.* Problèmes spécifiques, Rapport spécifique du GRECO, GRECO Publisher, Paris (in French).

Gary, G., and Zhao, H. (1996). ''Measurement of the dynamic behaviour of concrete under impact loading.'' *Proc., 2nd ISIS '96*.

Gopalaratnam, V., Gerstle, W., Isenberg, J., and Mindness, S. (1996). ''State-of-the-art report on dynamic fracture.'' *Rep.*, ACI Committee 446, American Concrete Institute, Detroit.

Hart, R., Cundall, P. A., and Lemos, J. (1988). ''Formulation of a three dimensional distinct element model—Part II. Mechanical calculations for motion and interaction of a system composed of many polyhedral blocks.'' *Int. J. Rock Mech. Min. Sci. and Geomech. Abstr.*, 25, 117–125.

Herrmann, H. J., Hansen, A., and Roux, S. (1989). ''Fracture of disordered, elastic lattices in two dimensions.'' *Physical Rev. B*, 39, 637–647.

Janach, W. (1976). ''The role of bulking in brittle failure of rocks under rapid compression.'' *Int. J. Rock Mech. Min. Sci. and Geomech. Abstr.*, 13, 177–186.

Liao, C. L., Chang, T. P., Young, D. H., and Chang, C. S. (1997). ''Stress-strain relationship for granular materials based on the hypothesis of best fit.'' *Int. J. Solids Struct.*, 34, 4087–4100.

Lindholm, U. S. (1964). ''Some experiments with the split Hopkinson pressure bar.'' *J. Mech. Phys. Solids*, 12, 317–335.

Lockner, D. A., and Moore, D. E. (1992). ''Microcrack interaction leading to shear fracture.'' *Rock mechanics*, Tillerson and Wawersik, eds., 807–816.

Magnier, S. A., and Donzé, F. V. (1998). ''Numerical simulations of impacts using a discrete element method.'' *Mech. Cohes.-Frict. Mat.*, 3, 257–276.
Magnier, S. A., Donzé, F. V., and Mareschal, J. C. (1997). ''Discrete element project, rapport d'activites 1997, le code 'Spherical Discrete Element' SDEC et ses applications.'' *Internal Rep.*, Montreal.
Müller, D. (1996). ''Techniques Informatiques Efficaces pour la Simulation de Milieux Granulaires par des Méthodes d'Eléments Distincts,'' PhD thesis, EPFL, Switzerland.
O'Connor, R. M. (1996). ''A distributed discrete element modeling environment algorithm, implementation and applications,'' PhD thesis, Massachusetts Inst. of Technol., Cambridge, Mass.
PFC3D (particle flow code in 3 dimensions), version 1.1. (1995). Itasca Consulting Group Inc. Minneapolis, Minn.
Rossi, P., Van Mier, J. G. M., Toutlemonde, F., Le Maou, F., and Boulay, C. (1994). ''Effect of loading rate on the strength of concrete subjected to uniaxial tension.'' *Mat. and Struct.*, 27, 260–264.
Schlangen, E. (1993). ''Experimental and numerical analysis of fracture processes in concrete,'' PhD thesis, Technische Universiteit Delft, Delft, The Netherlands.
Toutlemonde, F. (1995). PhD thesis, ENPC, France.
Walton, O. R. (1993). ''Numerical simulation of inclined chute of monodisperse, inelastic, frictional spheres.'' *Mech. of Mat.*, 16, 239–247.
Zhao, H., and Gary, G. (1996). ''On the use of SHPB techniques to determine the dynamic behavior of materials in the range of small strains.'' *Int. J. Solids Struct.*, 33, 3363–3375.

APPENDIX III. NOTATION

The following symbols are used in this paper:

$\tilde{A}_{\text{int}}$ = average surface where interaction is defined;
C = celerity of specimen's medium;
C_f = unloading velocity;
c = cohesion;
$D^{a,b}$ = D distance between centroids of two discrete elements a and b;
$D^{a,b}_{eq}$ = D_{eq} equilibrium distance between two discrete elements a and b;
$D^{a,b}_{\text{correction}}$ = correction distance for unloading;
D_{eq} = average equilibrium distance for all discrete elements;
$D_{\max}$ = maximum interaction distance;
E = Young's modulus;
e = local restitution coefficient;
$\mathbf{F}$ = interaction force vector;
$\mathbf{F}^{\text{a}}$ = total force acting on discrete element a;
$\mathbf{F}^{n}$ = normal interaction force vector;
$F^{n}_{\max}$ = maximum normal force;
$\mathbf{F}^{s}$ = shear interaction force vector;
$F^{s}_{\max}$ = maximum shear force;
$\mathbf{F}^{s}_{\text{reduced}}$ = updated shear force vector during slip;
$\mathbf{F}^{s}_{rot.1}$ = first rotation of shear interaction force vector;
$\mathbf{F}^{s}_{rot.2}$ = second rotation of shear interaction force vector;
F_{entrance} = entrance force at bar-specimen interface;
F_{exit} = exit force at bar-specimen interface;
$\dot{\mathbf{H}}$ = angular momentum vector of discrete element;
I = moment of inertia of discrete element;
K^n = interaction normal stiffness;
K^s = interaction shear stiffness;
k^a_n = normal stiffness of discrete element a;
k^a_s = shear stiffness of discrete element a;
l = number of applied forces on discrete element;
l_s = length of specimen;
$\mathbf{M}^a$ = **M** total moment vector acting on a discrete element a;
m = mass of element;
$\mathbf{n}$ = unit interaction vector;
n = number of interaction forces for discrete element;
R^a = R radius of discrete element a;
R_{init} = initial radius of all elements;
$R_{\max}$ = maximum possible radius size;
$R_{\min}$ = minimum possible radius size;
S_B = cross-sectional area of bar;
S_s = cross-sectional area of specimen;
T = maximum tensile strength;
V_{entrance} = entrance velocity at bar-specimen interface;
V_{exit} = exit velocity at bar-specimen interface;
$\dot{\mathbf{x}}$ = velocity vector of discrete element;
$\ddot{\mathbf{x}}$ = acceleration vector of discrete element;
x^a = component of position vector of discrete element a;
$\mathbf{x}^a$ = **x** position vector of discrete element a;
$\mathbf{x}^{a,b}$ = vector location of interaction point between a and b;
x^a_{mod} = modified component of position vector of discrete element a;
$\Delta\mathbf{F}^s$ = incremental interaction shear force vector;
Δt = integration time step;
$\Delta\mathbf{U}^s$ = shear displacement increment vector;
α = unloading factor;
β = softening factor;
γ = interaction range;
ε_i = strain of longitudinal incident wave;
ε_r = strain of longitudinal reflected wave;
$\dot{\varepsilon}_s$ = average strain rate imposed on specimen;
ε_t = strain of longitudinal transmitted wave;
ν = Poisson's ratio;
ρ = density of specimen;
σ_s = average stress imposed on specimen;
ϕ = friction angle;
$\boldsymbol{\omega}$ = angular velocity vector of discrete element;
$\dot{\boldsymbol{\omega}}$ = angular acceleration vector; and
$\bar{\boldsymbol{\omega}}$ = average angular velocity vector of two interacting discrete elements.